POLITECNICO DI TORINO
Repository ISTITUZIONALE

Drag reduction in a turbulent boundary layer with sinusoidal riblets

(Article begins on next page)

29 November 2022

Drag reduction in a turbulent boundary layer with sinusoidal riblets

Gioacchino Cafiero[a], Gaetano Iuso[a]

[a]*Dipartimento di Ingegneria Meccanica ed Aerospaziale, Politecnico di Torino, Corso duca degli Abruzzi 24, 10128, Torino (Italy)*

Abstract

We report on an experimental investigation on the effect of sinusoidal riblets on the near-wall characteristics of a turbulent boundary layer. The investigated riblets are characterized by a fixed wavelength and two different values of the amplitude. We comment on the flow field organization via hot wire anemometry, planar and stereoscopic particle image velocimetry experiments; furthermore, we infer on the friction drag, directly measured with a load cell, comparing the sinusoidal riblets to the reference case of riblets aligned with the mean flow (longitudinal riblets) and the Smooth case.

We show that the sinusoidal riblets generally yield higher drag reduction, attaining values as large as 10%, compared with the longitudinal riblets that are limited to 8% under the same conditions. We demonstrate that the drag reduction is associated with an overall attenuation of the turbulence intensity in the buffer layer. Furthermore, we provide statistical evidence of the fact that the sinusoidal riblets are responsible for an attenuation of the Reynolds shear stresses that contribute the most to turbulence production.

From the detection of the accelerated events in the buffer layer, we show that the sinusoidal riblets lead to a weakening of the intensity of the events in the streamwise plane and an enhancement of the spanwise induced motion. We relate this mechanism to that responsible for drag reduction when using spanwise wall oscillations, suggesting a possible effect of a secondary alternating vorticity in the grooves of the sinusoidal riblets.

Keywords:
Turbulent boundary layer, Flow Control, Drag reduction, Riblets

1. Introduction

The reduction of pollutants in the atmosphere is one of the main goals set by the ACARE Flightpath 2050. To this end, significant efforts are currently being spent by the fluid dynamics community to tackle the problem associated with the friction drag of airborne vehicles. Friction drag represents one of the most significant shares of drag exerted on aerodynamic bodies, typically contributing to about 50%. This has stimulated a wealth of control methodologies that can generally be split into two

different categories: active or passive. To the former belong those solutions that require energy, generally drawn from the engine bleed or from a dedicated power supply, with the drawback of increasing mass and costs.

The results obtained with these techniques are generally impressive, with large values of friction drag reduction. One example is that of the spanwise wall oscillations, yielding drag reductions as large as 40% as well as turbulence attenuation (Di Cicca et al., 2002a,b; Quadrio and Ricco, 2004). In a recent investigation Marusic et al. (2021) have shown that the power budget of this control methodology can be favourable depending on the characteristic actuation frequency. In particular, actuating the surface at frequencies comparable to those of the larger eddies that are located farther from the wall yields an energy efficient control, with drag reduction values that are incremental with the Reynolds number. However, this methodology requires rather complex systems to be implemented, which hinders application to real cases.

In realistic applications, it is not only the drag reduction achieved locally that is relevant, but also the persistence of such effects downstream of the forcing location (Cerutti et al. (2020)). Large scale forcing techniques, based on the generation of large scale vortices embedded in the near-wall region, have shown extremely promising results, featuring large friction drag reduction and turbulence attenuation, with possible implications also on the noise footprint of the turbulent boundary layer (Schoppa and Hussain, 1998a,b; Yao et al., 2018; Iuso et al., 2003; Iuso and Di Cicca, 2007; Cannata et al., 2020; Yao et al., 2021; Ji et al., 2021; Lee et al., 2021).

Despite providing the possibility of tuning the forcing parameters for the flow conditions, active flow control strategies require more complex and expensive systems to be manufactured and operated, also due to high maintenance costs. Furthermore, their effectiveness needs to be assessed against an energy budget to make sure that the benefit in terms of drag is not counterbalanced by the power supplied to the system (Spalart and Mclean, 2011; Quadrio, 2011).

In this sense, passive techniques represent a valid alternative to active ones, with typically lower friction drag reduction, but higher reliability and lower operative costs.

Examples of passive techniques are the use of large-eddy break-up (LEBU) devices, which showed interesting drag reduction (Walsh and Anders, 1989; Iuso and Onorato, 1995), despite being quite challenging to implement for aeronautics applications.

The main drawback of the passive techniques is that they are optimised for one working configuration only. It must be pointed out, though, that for typical aeronautical applications there is one flight phase that covers the majority of the flight envelope, which represents the design configuration, the cruise. In this sense, the use of winglets on aircraft wings represent a clear example ((Gehlert et al., 2021)).

One of the most attractive passive methodologies for friction drag reduction is that of the riblets, which are microgrooves operated on the surface and aligned to the freestream direction. The technique has already been applied to real cases, for example on swimsuits or America's Cup ships (NASA, 1993). The gains associated with the use of such geometries were so significant that they are now banned from these sports.

These techniques are typically characterized by lower drag reduction than the active ones, averaging 7-8% compared to the clean surface, but its applicability is generally much simpler as demonstrated by past and more recent applications (FreightWaves, 2021) on real aircraft. However, the complexity in the manufacturing of the

2

microgrooves represented a problem that could hardly be overcome. Recent advancements in carbon fibre materials have refuelled the interest in this technique.

The first studies on riblets date back to the 80s, as documented by the experimental work of Bechert et al. (1985); Bechert and Bartenwerfer (1989); Walsh (1980, 1982, 1983), followed by a wealth of numerical investigations (Choi, 1989; Luchini et al., 1991, 1992; Baron et al., 1993; Choi et al., 1993; Luchini, 1993; Luchini and Trombetta, 1995a,b; García-Mayoral and Jiménez, 2011; Ibrahim et al., 2021; Mele et al., 2020a,b; Modesti et al., 2021). The performance of the riblets was found to be highly dependent on the geometry of its cross-section, in particular the depth of the microgroove, the spacing between the grooves and their profile (blade, triangular, parabolic).

An extensive parametric study carried out by Bechert et al. (1997), where the effect of the geometry of the groove was carefully scrutinised, showed that blade riblets yield the highest drag reduction. Nevertheless, they would pose a problem both in terms of manufacturing and durability. Parabolic shaped profiles can represent a good trade-off between the performance and the ease of manufacturing.

A non-dimensional riblet spacing ($s^+ = su_\tau/\nu$, with u_τ being the friction velocity and ν the kinematic viscosity; with the superscript + we indicate the scaling in inner units) of approximately 15-16 yielded the highest values of drag reduction. More recently, García-Mayoral and Jiménez (2011) introduced a different dimensionless parameter, $l_g^+ = (A_g^+)^{1/2}$, accounting for the cross-section area (A_g^+) of the riblet profile as well. The authors showed that the highest drag reduction would be obtained for values of $l_g^+ \approx 11$.

The underlying mechanisms leading to drag reduction have been discussed in the literature by Choi (1989), Choi et al. (1993), García-Mayoral and Jiménez (2011), among others, mostly through highly resolved direct numerical simulation of several riblet geometries. The authors showed that the optimal value of the spacing corresponds to the condition where the near-wall structures cannot fit within the groove; hence, the structures are displaced towards the outer layers of the boundary layer. Near the wall, a region of nearly stagnating flow is then produced, with a corresponding reduction of the wall shear stress and skin friction drag.

Further improvements to the optimal riblet geometry have been proposed over the years. Bio-inspired geometries (Bechert et al., 2000), zigzag geometries (Sha et al., 2005) and wavy patterns (Peet et al., 2008; Peet and Sagaut, 2009; Kramer et al., 2010; Sasamori et al., 2014, 2017; Mamori et al., 2019). The latter solution is motivated by the possibility of enjoying the benefits brought by the riblet geometry, as well as those related to active flow control mechanisms, such as the spanwise oscillation of the wall (Choi, 2002), or forced by the tangential injection of air (Di Cicca et al., 2002a).

Kramer et al. (2010) tested a set of sinusoidal riblets characterized by different amplitudes and wavelengths. The microgrooves were operated on a square portion of a turbulent channel flow. The authors evidenced that, in this configuration, the sinusoidal riblets would not yield any appreciable drag reduction compared with the longitudinal ones. In that experiment, the effectiveness of the sinusoidal shape could have been hindered by the limited number of wavelengths of the sinusoidal pattern, which ranged from less than two to 7.5. In fact, such configuration is not deemed sufficient to ensure a fully developed manipulated turbulence close to the wall.

More promising were the investigations of Peet et al. (2008); Peet and Sagaut

(2009). A combined analytical and computational study suggested benefits of the wavy riblets up to 50% when comparing the skin friction drag to the longitudinal riblets when the wavelength of the sinusoidal shape is large enough. Incidentally, these values will be confirmed by the present experimental investigation. The authors attributed the performance enhancement of the wavy riblets to the transverse motion induced by the sinusoidal wall, in a similar fashion to that induced by the spanwise wall oscillation.

As demonstrated by the literature survey, riblets have been widely investigated for the last 30 years. The interest in the topic is far from being abated, considering the potential benefit brought by this passive manipulation. Recent interest of aircraft manufacturers in implementing the technology on existing aircraft (Airbus, 2019) has fueled the research to find innovative and even more efficient solutions. Despite showing interesting results, an experimental description of the near-wall structure stemming from the wavy modification of the wall has not been performed yet. Furthermore, an experimental investigation with a sufficient number of wavelengths of the sinusoidal pattern is still lacking.

In this manuscript, we aim at providing further insights to fill this gap, through the experimental investigation of a zero pressure gradient turbulent boundary layer manipulated with wavy riblet geometries. We can introduce the wall manipulations by replacing a portion of the wall with either a riblet plate with longitudinal or sinusoidal patterns. We perform direct measurements of the friction drag, to obtain a global understanding of the drag reduction yielded by the wavy patterns. Furthermore, hot wire anemometry and planar and stereoscopic particle image velocimetry provide statistical and spectral information to carry out a comparative study between the investigated cases.

2. Experimental apparatus

The experiments were performed in an open circuit wind tunnel at Politecnico di Torino. The tunnel has a settling chamber containing honeycomb and mesh screens, followed by a contraction with area ratio of 3:1, leading to a test section 5300 mm long and with a cross-section area of 500 mm x 700 mm.

The flat plate where the investigated boundary layer develops is located at mid-height of the test section and extends from side to side, thus effectively reducing the cross section area to 500 mm x 350 mm. This reduction is obtained through a contoured contraction. The purpose of this is twofold: first it avoids any sharp area variation, which would disrupt the quality of the flow. Second, it allows for the insulation of the bottom portion of the test section which is used for the plate positioning system. A trip wire is placed at the start of the flat plate to trigger an early transition to a turbulent boundary layer.

A portion of the flat plate of size 260 mm x 260 mm is hollow and allows for the insertion of different plates. The correct alignment of the tested plate with respect to the remaining portion of the flat plate is ensured with micrometric accuracy through the possibility of controlling the height and the inclination of the tested plate. In particular, the height is controlled using a laser optical displacement measurement optoNCDT 1320-25 manufactured by Micro-Epsilon with a measurement error to within $2.5\mu m$, corresponding to 0.13 wall units in the worst case scenario of largest Reynolds number,
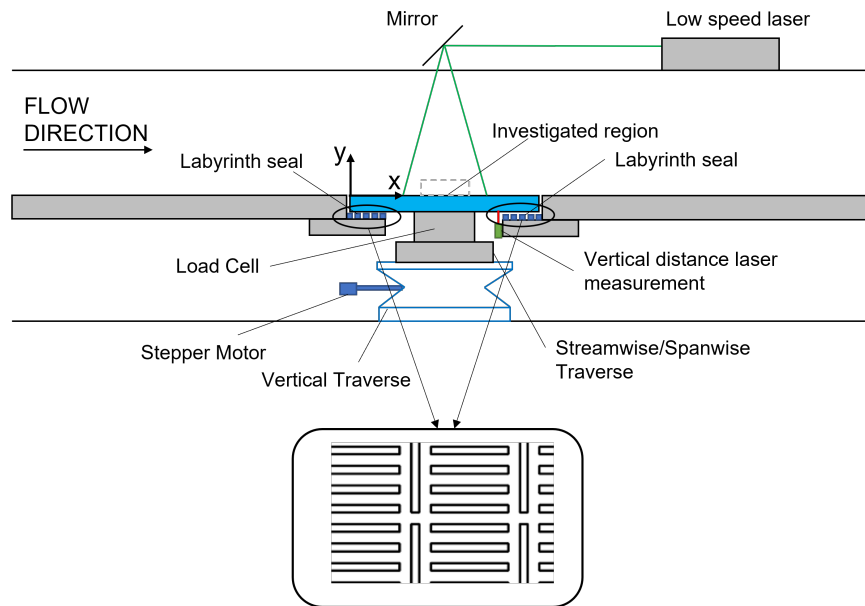
Figure 1: Schematic representation of the test section with detail of the removable plate. In the insert, detail of the labyrinth seal located beneath the plate.

or less than 10% of the groove height h. The inclination of the plate is checked through a high precision digital inclinometer (measurement error to within 0.1°).

The peaks of the riblet profiles are set at the same height as the flat plate, hence the test surfaces are recessed, that is, the virtual origin of the boundary layer lies below the smooth wall. The vertical positioning of the riblet plate is changed with micrometric accuracy using a stepper motor. The reading of the laser displacement measurement is considered as the datum.

The comparative study between different tested plates is carried out by placing each of the tested plates in the test section. The investigated plates are mounted on the load cell which in turn is placed on a positioning system secured to the lower wall of the test section. The positioning system allows the micrometric movement of the plate in the streamwise (x), spanwise (z) and vertical (y) direction. The plates are connected to a three-axis load cell (K3D40 ME-System, characterized by ± 2N FS corresponding to ± 4mv of electric output when operated at 10Volt) measuring forces which are aligned with x, y and z, respectively. An in-house calibration tailored to the typical range of friction forces experienced in this work, was performed using a high-class precision balance (Kern Tab 20-3) with FS =20gr, and accuracy of 0.001gr.

A sketch of the experimental set up is reported in Figure 1. The reference frame that will be used through the paper is also indicated in Figure 1, with the origin located at the wall, x aligned with the streamwise direction, y aligned with the wall normal direction and z is defined according to the right hand rule.

Four different plates were investigated: a flat plate, a riblet plate with longitudinal
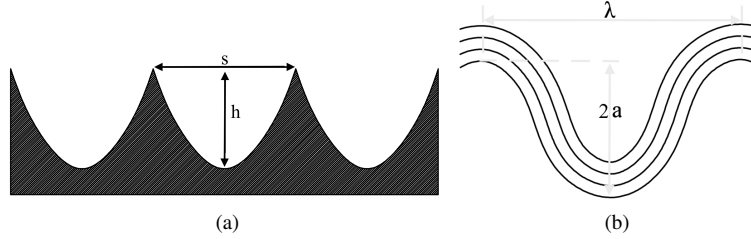
5

Figure 2: Detail of the parabolic profile of the grooves. a) Streamwise cross-sectional view and b) Plan view of a generic sinusoidal grooved surface.

grooves (RLONG), two riblet plates with sinusoidal grooves (RS1 and RS2). Each one of the tested plates is a square having side of 258 mm and thickness of 10 mm. This leads to a small gap between the edge of the tested plate and the flat plate. A labyrinth seal (see Figure 1b) was mounted underneath the plate to avoid any leakage through the gap between the tested plate and the surrounding flat plate.

The three riblet plates are characterized by the same groove profile, having parabolic shape. The choice of the cross-section shape was a compromise between the triangular and the blade configuration. In fact, while the triangular riblets pose lower maintenance problems with respect to the blade riblets, the blade shape caters for higher drag reduction (Bechert et al., 1997). It must be noted that the triangular riblets provide significant technological challenges to manufacture the sharp internal corners. It is worth explicitly mentioning that given the impossibility of reproducing a sharp apex, a curvature radius of $r = 10\mu m$ was deemed as acceptable during the manufacturing process. This value, rescaled in inner units, ranges from 0.23 to 0.52 viscous units.

The height of the groove is $h=210\mu m$ whilst the spacing between two grooves is $s=300\mu m$, thus resulting in a h/s ratio equal to 0.7 (see Figure 2a). The two sinusoidal riblets are characterized by the same wavelength λ=19.2mm, thus leading to at least N_λ=13 wavelengths on the tested plate. The wavelength was defined to obtain values of $\lambda^+ = O(10^3)$, considering the typical friction velocity that can be achieved in the wind tunnel. Conversely, two different values of the semi-amplitude a are considered (see Figure 2b), with a=0.15mm in the RS1 and a=0.6mm in the RS2 case, respectively. A summary of the geometric parameters of the riblet plates is reported in table 1, and their values rescaled in inner units are reported in table 3.

The riblet performance is strongly dependent on the spacing normalised in inner units $s^+ = s/l_\tau$, where $l_\tau = \nu/u_\tau$ is the viscous lengthscale, ν the air kinematic viscosity and u_τ is the friction velocity. Since the manufacturing of the riblet plates can be expensive, we vary s^+ by changing the Reynolds number, which results into a variation of the friction velocity.

The freestream speed U_∞ is regulated using an inverter and measured using a Pitot tube located at the inlet of the test section and connected to a pressure transducer Setra 239C having a full scale (FS) of 0.2psi and an accuracy of ±0.14% FS. The typical error on the freestream speed ranges from ±4% at the lowest speed to less than ±1% at the highest speed. Four different values of the asymptotic speed are considered,

6

	RLONG	RS1	RS2
s (mm)	0.30	0.30	0.30
h (mm)	0.21	0.21	0.21
h/s	0.70	0.70	0.70
a (mm)	0	0.15	0.60
λ (mm)	∞	19.2	19.2
N_λ	N.A.	13	13

Table 1: Geometric data for the riblet plates.

$U_\infty(m/s)$	u_τ	Re_τ	Re_θ	$\delta(mm)$	$l_\tau(\mu m)$	H
8.30	0.36	1050	2200	44.9	42.5	1.36
13.4	0.53	1210	2900	34.5	28.4	1.34
17.9	0.65	1235	3900	28.3	23.1	1.38
22.0	0.79	1470	4900	26.3	19.2	1.38

Table 2: Experiment details: value of the asymptotic speed U_∞, friction velocity u_τ from the Clauser chart method, Reynolds numbers based on friction velocity Re_τ and momentum thickness Re_θ, boundary layer thickness δ, viscous lengthscale l_τ and boundary layer shape factor H. All the quantities are measured in the Smooth plate case, in the middle of the plate

.

thus resulting in a range of friction Reynolds numbers ($Re_\tau = u_\tau\delta/\nu$, with δ being the boundary layer thickness) from 1050 to 1470, calculated in the middle of the plate. Details of the experiment conditions are listed in table 2. The value of the local friction velocity u_τ is obtained from a Clauser fit to the logarithmic portion of the mean flow profile (using as values of the constants $k = 0.41$ and $B = 5.2$). The results were also compared with the value obtained from the load cell measurements, u_τ^{LC}, showing that the maximum difference between the two approaches is 8% at $Re_\theta = 2200$ and 3% at $Re_\tau = 4900$. In the following we consider the local value of the friction velocity obtained using the Clauser chart method to normalise the quantities in inner units.

2.1. Velocity measurement techniques

The flow field was characterized using hot wire anemometry (HWA) and low speed Particle Image Velocimetry (PIV). The choice of performing both measurements came

Re_θ	a^+ RS1	a^+ RS2	λ^+	s^+
2200	3.53	14.1	452	7.06
2900	5.28	21.1	676	10.6
3900	6.49	25.9	830	13.0
4900	7.81	31.3	1000	15.6

Table 3: Riblets' geometry normalised in inner units at the four values of the Reynolds number.

Re_θ	l^+	d^+	$t_a U_\infty/\delta$	$t^+ = t_a u_\tau^2/\nu$
2200	29	0.12	11000	0.42
2900	44	0.18	23000	0.93
3900	54	0.22	37000	1.39
4900	65	0.26	50000	2.08

Table 4: Hot wire anemometry experiments details. The hot wire probe is characterized by $l = 1.25mm$ and $d = 5\mu m$, hence $l/d = 250$. The data in the table is rescaled in inner variables. The boundary layer turnover time is rounded to the leading order.

Re_θ	Δx^+	Δy^+	$\Delta x/\delta$	$\Delta y/\delta$	$\Delta t(\mu s)$	y^+_{min}	IW^+
2900	820	760	0.68	0.63	15	10	7.32
3900	1005	940	0.82	0.63	10	12	9.00
4900	1210	1125	0.84	0.78	6	20	10.8

Table 5: PIV and stereo-PIV experiment details. The extent of the field of view is normalised both in inner and outer variables. Δt indicates the time delay between the two frames. IW^+ gives the value of the interrogation window rescaled in inner units.

from the necessity of enjoying the spatial information delivered by PIV and the temporal information which is instead provided locally by HWA.

In the HWA experiments, the velocity signal is measured using a one component hot wire probe driven by a Dantec DISA constant temperature anemometer (CTA). The hot wire was operated with an overheat ratio of 0.8. The sensing length of the wire is $l \approx 1$ mm, corresponding to $l^+ \approx 40$ whilst the wire diameter is $5\mu m$. As indicated by Hutchins et al. (2009), this value of l^+ may lead to the modulation of the streamwise turbulence intensity. We accepted this problem considering that we had the comfort of the high resolution PIV measurements. Furthermore, the modulation effect depends on the Reynolds number that in turns influences the viscous length and, as a consequence, the sensor's length in wall units. This suggests that the modulation effect at fixed value of the Reynolds number is the same for all the cases, hence it does not harm the comparative study carried out in the present investigation.

Data are sampled at a frequency of 20 kHz using a 16-bit National Instruments NI-9215 data acquisition board. Each measurement lasts for t_a=60s; this time corresponds to a number of boundary layer turnover times $t_a U_\infty/\delta$ of 11,000 at $Re_\tau = 1050$ and 50,000 at $Re_\tau = 1470$. This was estimated to be a sufficiently long time for convergence of the turbulent statistics as well as the velocity spectra studied here. The experimental conditions for the HWA experiments are listed in table 4.

The spatial organization of the flow was investigated through both low speed planar PIV and stereoscopic PIV (stereo-PIV).

A Dantec Dynamics Nd:YAG Dual Power 200 laser (200 mJ/pulse energy, 15 Hz repetition rate) operated in dual pulse mode was used to illuminate the tracing particles. The laser was mounted on the roof of the wind tunnel and an optical path constituted by a spherical and a cylindrical lens shaped the laser beam into a thin sheet with thickness

of about 0.7 mm. A 2 inches mirror was used to direct the laser sheet towards the test section and to align it with the *xy* plane. The illuminated region extended for about 25 mm in the streamwise direction.

One Andor Zyla 5.5Mpix sCMOS camera (sensor size of 2560x2160 pixels, with pixel size of 6.5 μm) was used to capture the images of the tracing particles. The camera was synchronized with the laser system and operated in double exposure mode. The acquisition frequency was set to 15 Hz. The camera was equipped with a Nikon 200mm Micro lens, operated at a value of the aperture $f_\# = 11$. The imaged area extended for 23x21 mm in the $x - y$ plane, corresponding to a spatial resolution of approximately 80 pix/mm. The corresponding value in inner units along with other relevant information about the PIV experiments are reported in table 5.

The stereoscopic PIV measurements were performed using two Andor Zyla 5.5Mpix sCMOS cameras arranged on one side of the wind tunnel to image the same area of the PIV case. The cameras were equipped with Scheimpflug mounts and two Nikon 200mm Micro lenses, operated at $f_\# = 11$ and the resulting digital resolution was the same of the PIV case. The geometric calibration was performed using a home-made target with black dots and white background, with dots spacing equal to 2.2mm. The geometric calibration was performed using the pinhole Tsai method (Tsai, 1987). The residual calibration error was below 1 pixel. The calibration was then further corrected through a self-calibration process (Willert, 1997; Wieneke, 2005; Giordano and Astarita, 2009; Wieneke, 2018) that allowed to reduce the calibration error to 0.1 pixel.

The flow was seeded upstream the stagnation chamber using HAZEBASE fluid. The liquid droplets of 1 μm in diameter were generated using a Safex Fog generator FOG 2010. For each Reynolds number and each plate 2000 double exposure images were acquired. The raw images were pre-processed to reduce to a minimum the reflection of the laser onto the flat plate. The Proper Orthogonal Decomposition based approach, as proposed by Mendez et al. (2017), allowed for a significant attenuation of the laser reflection. Nevertheless, the particles in the vicinity of the plate were still affected by some residual spurious reflection. The laser reflection was even more intense in the case of the rough walls, as the light was non uniformly scattered. Every effort was spent to reduce this effect to a minimum and to ensure that only a limited portion of the near wall flow field would be affected by the reflection. Table 5 shows the wall normal distance, in inner units, of the first velocity vector not affected by the laser reflection in the PIV and Stereo-PIV measurements.

The vector fields are obtained by processing the particles' images using a correlation based algorithm. A spline interpolation of the image and of the velocity field was performed, as recommended by Astarita (2006, 2008). A Blackmann weighting window was used to tune the spatial resolution (Astarita, 2007). The algorithm is based on a multi-pass approach and the final interrogation window size was 16x16 pix, with 87.5% overlap. The corresponding values rescaled in inner units are reported in table 5.

2.2. *Flow validation*

We first focused on the validation of the boundary layer flow in the case of the Smooth plate. We checked the boundary layer statistics, to ensure that they would
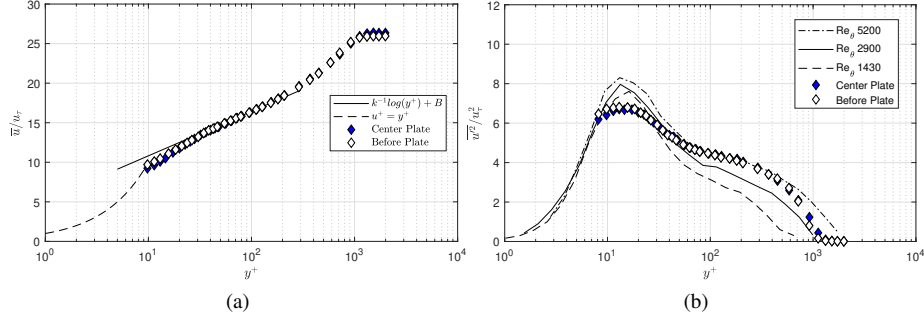
Figure 3: a) Mean streamwise velocity component ($\overline{u}/u_\tau$) and b) the variance of the streamwise velocity ($\overline{u'^2}/u_\tau^2$) plotted against the wall normal coordinate re-scaled in inner units y^+. The data was collected at $Re_\theta = 3900$.

agree well with the typical scaling reported in the literature, thus confirming the effectiveness of the labyrinth seal surrounding the plate with no appreciable differences before and after the gap. HWA measurements were taken at two different locations: 50 mm upwind the gap and in the middle of the tested plate (i.e. 130 mm downwind the gap). Figure 3 shows the mean streamwise velocity component ($u^+ = \overline{u}/u_\tau$, with u_τ being the friction velocity of the Smooth plate) and the variance of the streamwise velocity ($\overline{u'^2}/u_\tau^2$) plotted against the wall normal coordinate rescaled in inner units y^+. The data was collected at $Re_\theta = 3900$.

The mean velocity profiles u^+ measured before and at the centre of the plate exhibit the same behaviour. In particular, both profiles follow a logarithmic law in the range of y^+ between 30 and 200. The continuous line is representative of the canonical log-law, $u^+ = \frac{1}{k} log(y^+) + B$ with the values of the constants $k = 0.41$ and $B = 5.2$.

At smaller values of the wall normal coordinate, $y^+ < 15$, the measured data approach the velocity profile predicted in the viscous sublayer, $u^+ = y^+$.

The streamwise velocity variance profiles ($\overline{u'^2}/u_\tau^2$) measured at $Re_\theta = 3900$ are compared to the data obtained by De Graaff and Eaton (2000), with values of Re_θ ranging from 1430 to 5200. It is clear how there is no effect of the gap on the variance profiles. The $\overline{u'^2}/u_\tau^2$ profiles feature an inner peak at $y^+ \approx 13$, as widely documented in the literature. The value of the peak should show little dependence on the Reynolds number. The underestimation of the peak compared to the literature data is attributed to the length of the wire l^+ (Hutchins et al., 2009) as reported in table 4. As the wall normal coordinate increases, the streamwise velocity variance shows a monotonic decrease that is approaching a plateau in the range of $80 < y^+ < 140$, consistently with the value of Re_τ.
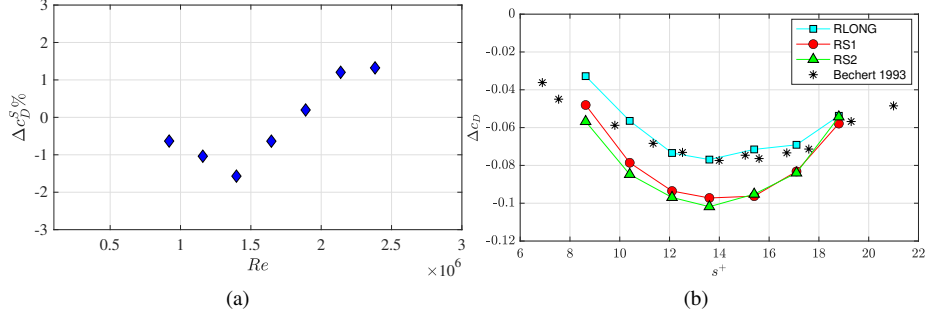
Figure 4: a) Difference between the drag coefficient measured in the Smooth case as a function of the Reynolds number and the corresponding value stemming from the application of the empirical *one-fifth* law, $\Delta c_D^S\%$. b) Drag variation Δc_D as a function of the non dimensional spacing rescaled in inner units s^+. Data are to be considered with a ±1.8% uncertainty bar.

3. Results

3.1. Load cell measurements

The load cell measurements allow to draw global conclusions about the overall drag reduction attainable with the sinusoidal riblets. As detailed in the previous section, we investigated a range of s^+ by changing the value of the inlet Reynolds number, thus effectively changing the value of u_τ.

We first focused on the validation of the load cell measurements. Data obtained for different values of the Reynolds number are reported in Figure 4a in terms of percentage difference between the drag coefficient of the smooth plate, c_D^S, and well known scaling for a zero pressure gradient boundary layer $c_D^e = 0.074Re^{-1/5}$:

$$\Delta c_D^S\% = \left(\frac{c_D^S}{0.074Re^{-1/5}} - 1\right) \tag{1}$$

The results show that there is a good agreement of the experimental data with the empirical laws across the investigated range of Reynolds number, limited to ±1.8%.

In Figure 4 we show the values of the drag variation $\Delta c_D = (c_D - c_D^S)/c_D^S$ as a function of the non dimensional spacing s^+ rescaled in inner units. We also report the results obtained with the longitudinal riblets by Bechert et al. (1997).

The RLONG data show a good agreement with the results from Bechert et al. (1997), for values of $s^+ > 10$. The discrepancies that can be detected at $s^+ = 8$ are most likely to be attributed to the fact that the wind tunnel has a minimum working speed at which the flow is steady in the test section. Furthermore, at lower values of the freestream speed, the load cell is affected by larger uncertainties, since the friction drag reduces.

Both RS1 and RS2 feature larger values of drag reduction. However, all the riblet cases attain the maximum drag reduction at $s^+ \approx 13$. The RS2 case seems to lead to slightly larger drag reduction, however, it must be pointed out that the differences between RS1 and RS2 are small enough to be considered within the measurement

11

error. Peet and Sagaut (2009) found, from theoretical arguments, that sinusoidal riblets with a triangular profile could cater for drag reductions of 7%; this value could be increased to 13% in the case of blade riblets, thus suggesting a dependence on the riblet profile. The intermediate value of 10% that is found in the present investigation can be then justified by the employed parabolic shape, which lies in between the blade and triangular geometry.

The results show that the sinusoidal riblets can lead to a further drag reduction of roughly 2.5%, which is in line with the analytical prediction reported by Peet and Sagaut (2009), who suggested that the long wavelength sinusoidal riblets could be responsible for a further drag reduction roughly equal to 50% of the one catered by the longitudinal one. We seek justification for this in the flow field organisation, as detailed in the following sections.

It is worth pointing out, though, that the choice of wavelength λ for the riblet geometry was based on the typical lengthscale of the near wall streaks. At $s^+ = 13.5$, corresponding to the maximum drag reduction, the wavelength λ normalised in wall units is 830, which is close to the typical value of 1000 for the near wall streaks (see also table 3). We deem this passive forcing as particularly efficient since it tampers with the near wall turbulence generation cycle by interfering with the high speed and low speed streaks.

Moreover, a comparison can be drawn with the periodic spanwise oscillation, as suggested also by Peet and Sagaut (2009), by estimating an equivalent period of oscillation. In fact, considering a convective velocity $c^+ =10$ at $y^+=10$, we estimate a period of oscillation in inner units, $T^+ \approx 86$, which is close to the optimal value of $T^+=100$, found to be the condition yielding the maximum drag reduction (Baron et al., 1993; Choi, 2002).

3.2. Flow field statistics

We start by showing in Figure 5 the comparison of the mean streamwise velocity profiles obtained with HWA for the different cases of RLONG, RS1 and RS2. The values of the Reynolds number are reported in table 4, and the value of u_τ used to normalise the data is obtained with the Clauser chart method applied to each case. As discussed at length in the literature (Jimenez, 2004; García-Mayoral and Jiménez, 2011), an upward shift of the mean velocity profile (ΔU^+) corresponds to a drag reduction.

At the lowest value of Re_θ, only little differences emerge from the comparison of the four plates. In particular, the onset of the effects of the wall manipulation requires a sufficient number of wavelengths, or an adjustment length, to match the global values of drag measured with the load cell. The velocity profiles data collected at different streamwise locations on the ribbed plate provide us with an indication of the location beyond which the boundary layer will be in equilibrium. This data, not included in the manuscript for the sake of conciseness, suggest that beyond $x/\delta = 2.5$ (or $\approx 4\lambda$) the manipulated boundary layer can be considered in equilibrium.

Increasingly larger values of the local Reynolds number lead to a progressive increment of the drag reduction. The behaviour is not monotonic, though. The highest efficiency of the riblet geometry, evaluated in terms of the shift of the logarithmic region, is obtained at $Re_\theta=3900$ (corresponding to $s^+ \approx 13$). A further increment of the
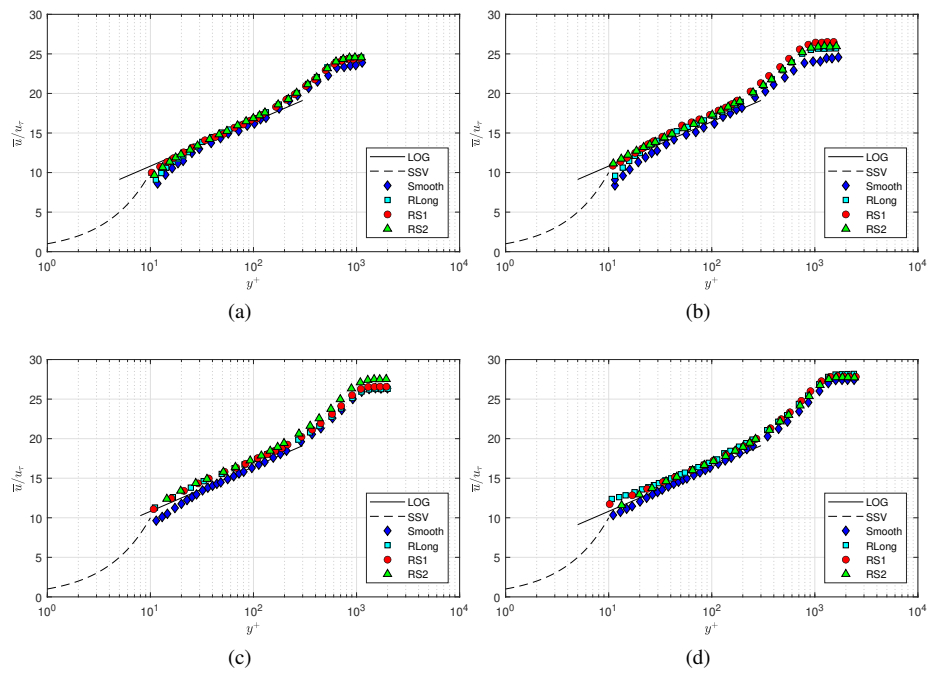
Figure 5: Mean streamwise velocity component ($\overline{u}/u_\tau$) plotted against the wall normal coordinate re-scaled in inner units y^+. The values of the Reynolds number are: a) $Re_\theta = 2200$, b) $Re_\theta = 2900$, c) $Re_\theta = 3900$ and d) $Re_\theta = 4900$. The data was collected at the centre of the plate.
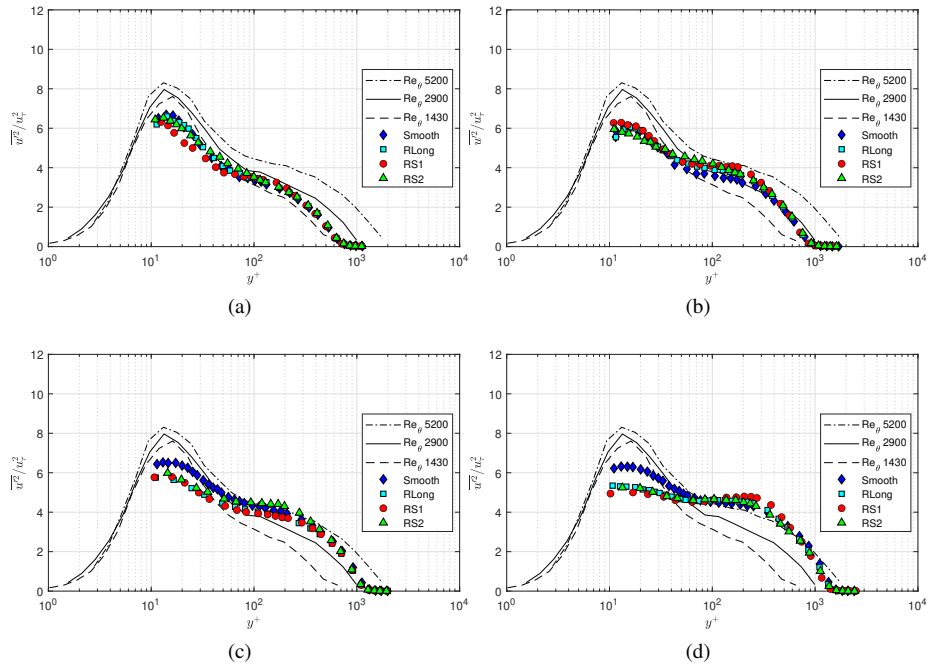
Figure 6: Variance of the streamwise velocity component ($\overline{u'^2}/u_\tau^2$) plotted against the wall normal coordinate re-scaled in inner units y^+. The values of the Reynolds number are: a) $Re_\theta = 2200$, b) $Re_\theta = 2900$, c) $Re_\theta = 3900$ and d) $Re_\theta = 4900$. The data was collected at the centre of the plate. Reference values from De Graaff and Eaton (2000) are also reported for three values of the Reynolds number.

14

Reynolds number (Figure 5d, $Re_\theta = 4900$), effectively consisting in a different value of s^+, does not yield further drag reduction. This is in good agreement with the load cell measurements and the typical behaviour that is exhibited by riblet surfaces. At larger values of s^+, the riblet is not effective anymore, transitioning to a rough wall behaviour (Bechert et al., 1997; Jimenez, 2004).

The effect of the riblet geometry on the variance of the streamwise velocity evidences significant differences only for values of Re_θ equal to 3900 and 4900 (Figure 6c-d). The data from De Graaff and Eaton (2000) obtained in a turbulent boundary layer on a Smooth wall for a range of Re_θ between 1430 and 5200 is also reported as a reference.

For the sinusoidal riblets, at smaller values of the Reynolds number (Figure 6a-b), the attenuation is much more limited and is confined to the range of y^+ between the buffer layer and the log layer. Furthermore, regardless of the value of the Reynolds number, the riblets are also characterized by a displacement of the turbulence intensity towards the outer regions of the boundary layer, as evidenced by the increase of the turbulence intensity at $y^+ = 200$. As already mentioned in the previous sections, the modulation of the turbulence intensity peak emerging from the comparison with the data from De Graaff and Eaton (2000) stems from the value of l^+ of the hot wire probe (see 4). Nevertheless, this does not hinder the comparative study between the Smooth and riblet geometries.

It is interesting to notice that the behaviour of the inner peak (occurring for values of $y^+ \approx 12$) does not show the same behaviour of the drag reduction. It can be seen how the turbulence intensity peak monotonically decreases with increasing values of the Reynolds number. This difference could be related to the mechanism leading to the drag reduction associated with the sinusoidal riblet geometry, and that will be detailed further in the next sections. At the largest value of Re_θ the riblet geometry provides the maximum attenuation of the turbulence intensity peak, although the maximum drag reduction is achieved at $Re_\theta = 3900$.

The in-plane component of the Reynolds shear stress $\overline{u'v'}$ normalised in inner units is reported in Figure 7 for three different values of the Reynolds number, namely $Re_\theta = 2900$, $Re_\theta = 3900$ and $Re_\theta = 4900$. The data is obtained with the planar PIV measurements.

The Smooth case shows, irrespective of the value of Re_θ, a peak that is located in the log-layer at approximately $y^+ = 150$. The riblet cases show instead a much stronger dependence on the Reynolds number, as expected. All the cases feature significant reductions of the Reynolds shear stresses in the buffer layer, with the RS1 featuring the strongest attenuation, with values as large as 25% at $y^+ = 15$ and $Re_\theta = 2900$. The RS2 case is characterized by values of the Reynolds stress that are similar to those of the RLong in the buffer layer.

At larger values of y^+ the RS1 at $Re_\theta = 3900$ and 4900 exhibits values of $\overline{u'v'}$ at least as large as the Smooth case. Despite showing lower attenuation near the wall, the RLong and RS2 cases are instead characterized by lower values of $\overline{u'v'}$ across the log layer.
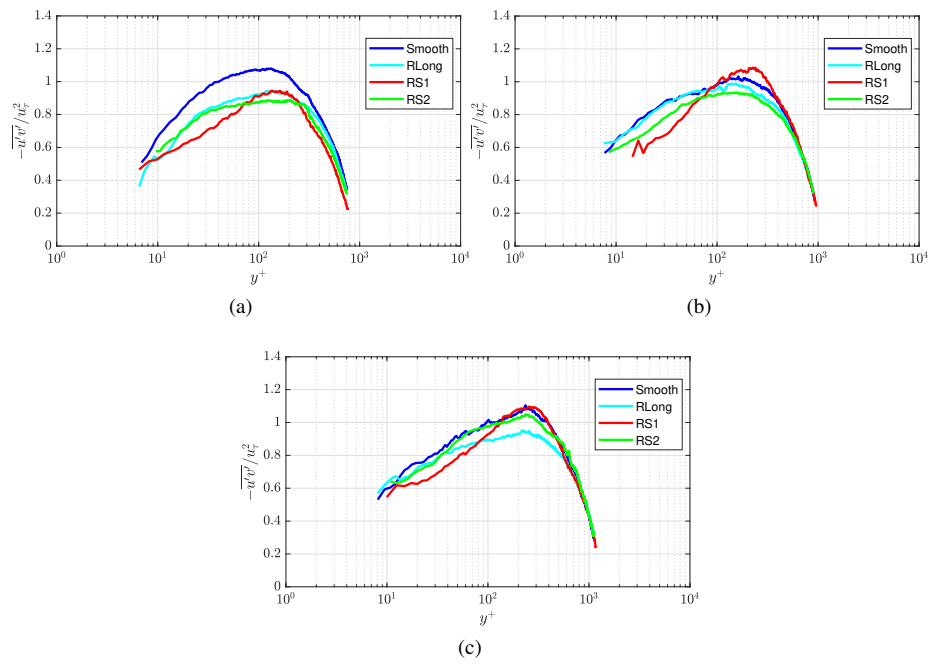
15

Figure 7: In-plane Reynolds shear stress component, $\overline{u'v'}$ normalised in inner units and plotted as a function of the wall normal distance for the Smooth, RLONG, RS1 and RS2 cases at a) $Re_\theta = 2900$, b) $Re_\theta = 3900$ and c) $Re_\theta = 4900$.
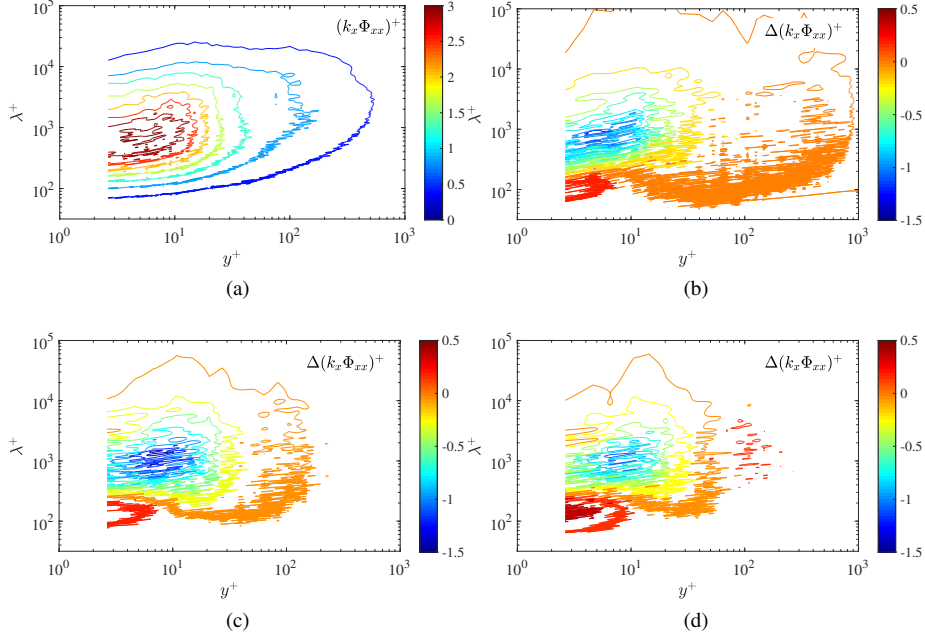
Figure 8: Pre-multiplied streamwise velocity spectra $(k_x\Phi_{xx})^+$ plotted in the wall normal distance (y^+) - wavelength (λ_x^+) plane. To improve readability, the RLong (b), RS1 (c) and RS2 (d) cases are shown as difference with respect to the smooth case.

3.3. Velocity spectra

In order to reveal the effect of the riblet geometry on the organization of the energy containing structures across the boundary layer, the contour plots of the pre-multiplied velocity spectra ($k_x\Phi_{xx}$, being $k_x = 2\pi/\lambda_x$ the longitudinal wavenumber, λ_x the streamwise wavelength and Φ_{xx} the streamwise velocity spectra) are reported in Figure 8. The data is plotted for a representative value of the Reynolds number ($Re_\theta = 3900$, corresponding to the maximum value of the drag reduction) in the wavelength-wall normal distance plane and normalized in inner units. To highlight the differences between the investigated cases, the RLong (b), RS1 (c) and RS2 (d) cases are shown as difference with respect to the smooth case, $\Delta(k_x\Phi_{xx})^+$.

The Smooth plate evidences a maximum centred at $\lambda_x^+ \approx 1000$ extending for a broad range of scales across the buffer layer. The high energy associated with this range of wavelengths is interpreted as a signature of the presence of the near wall streaks, whose typical length is of the order of 1000 viscous units (Di Cicca et al., 2002a; Ganapathisubramani et al., 2005; Hambleton et al., 2006; Herpin et al., 2013).

Figures 8b-d show a significant attenuation of the turbulence activity across the buffer layer for the riblet geometries. In particular, both the maximum value and the extent of the region characterized by high intensity is significantly reduced at about $\lambda_x^+ \approx 1000$, particularly for the sinusoidal cases. This suggest that the energy distribution across the different scales is influenced by the surface conditions, and this effect is
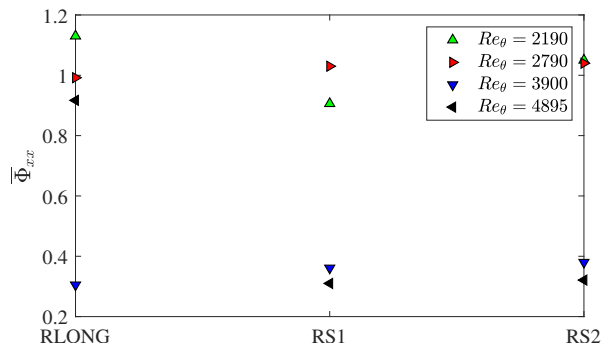
17

Figure 9: Integral of the spectral energy calculated in the range of wall normal distances $5 < y^+ < 20$. Data are normalised with respect to the energy of the Smooth case.

most significant in the near-wall region.

The attenuation of the spectral energy across the buffer layer is confirmed in Figure 9 where we plot the integral of the spectra for a range of wall normal distances $y^+_{min} < y^+ < y^+_{max}$ and then averaged over the wavenumber k_x,

$$\overline{\Phi}_{xx} = \int_{y^+_{min}}^{y^+_{max}} (k_x \Phi_{xx})^+ dy^+ \tag{2}$$

where $y^+_{min} = 5$ and $y^+_{max} = 20$ indicate the beginning and the end of the buffer layer, respectively. The data shows the value of the spectral energy normalised with respect to the Smooth case. At values of $Re_\theta = 2200$ and $Re_\theta = 2900$ the geometry manipulation does not lead to any significant attenuation of the energy contained in the buffer layer. Conversely, at $Re_\theta = 3900$ all the riblet cases feature values of energy of about 30% compared to the Smooth case, as also evidenced when commenting Figure 6. It is interesting to notice that the sinusoidal riblets keep the same value of attenuation also at the largest value of Re_θ, whereas the RLONG case recovers values similar to the Smooth plate.

The results obtained with the sinusoidal riblets are encouraging, as they demonstrate that this geometry manipulation can still keep satisfying levels of energy attenuation even at larger values of the Reynolds number.

3.4. Quadrant analysis

The joint probability distribution function (jPDF) $P(u', v')$ has been calculated at a fixed wall normal distance, $y^+ = 30$ and $Re_\theta = 3900$. The jPDF have been calculated also at different values of the wall normal location, $y^+ = 20$ and $y^+ = 40$, without any significant difference on the conclusions drawn below. This technique, generally referred to as quadrant analysis (Wallace, 2016), highlights how the velocity fluctuations are distributed across the four quadrants and how they participate into building up sweep (Q4) and ejection (Q2) events.

The comparison between the investigated cases is carried out considering one generic contour level of the jPDF for all the cases, namely $P(u', v') = 0.006$. As expected, the
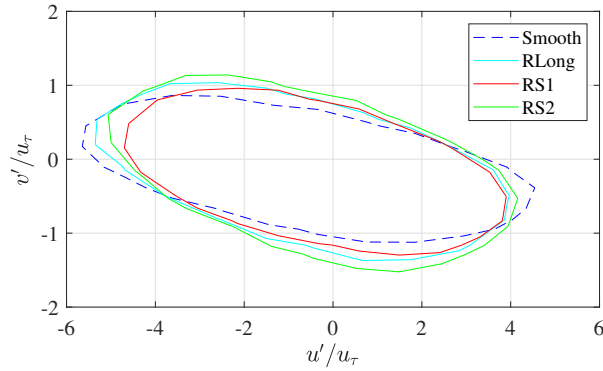
Figure 10: Joint probability distribution function, $P(u', v')$, at $y^+ = 30$ and $Re_\theta = 3900$. One generic contour level is selected for all the cases, namely $P(u', v') = 0.006$.
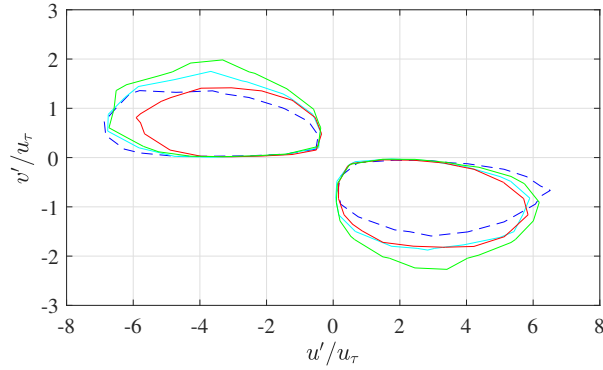

Figure 11: Weighted joint probability distribution function, $u'v'P(u', v')$, at $y^+ = 30$ and $Re_\theta = 3900$. One generic contour level is selected for all the cases, namely $u'v'P(u', v') = -0.003$.

jPDF show a preferential direction, that is aligned along the quadrants Q2 and Q4, with only limited energy associated with the quadrants Q3 and Q1. That is irrespective of the specific case.

However, it is interesting to see how the wall manipulation, in particular the sinusoidal one, modifies the jPDF, progressively reducing the probability of occurrence of events with large velocity fluctuations in the streamwise direction. This is particularly evident in the RS1 case. The wall normal velocity fluctuations appear instead intensified with respect to the smooth case for all the ribbed surfaces.

Conversely, the RLONG case features a jPDF that is characterized by similar values of the velocity fluctuations, suggesting only minimal differences in the way they are distributed. The RS1 case is the one showing the largest differences, with a significant attenuation of the boundaries of the jPDF. Similar observations can be drawn for the RS2 case, with a larger scatter than the RS1 case.

The analysis can be further detailed by analyzing those components of the velocity fluctuations that contribute the most in building up the Reynolds shear stress and

the sweeps and ejections events. The weighted jPDF $u'v'P(u', v')$ reported in Figure 11, provides further evidence of the attenuation of the values of the Reynolds shear stress. Also in this case, the comparison between the investigated cases is carried out considering one generic contour level of the jPDF for all the cases, namely $u'v'P(u', v') = -0.003$. In the Smooth case, the peak is broader in the streamwise direction than the manipulated case both in the Q2 and Q4, thus suggesting the contribution of more energy containing events to the turbulence production. Conversely, for all the riblet cases and in particular for the RS1, the peaks are closer to the origin, evidencing an attenuation of the velocity fluctuations that participate into producing the turbulence. This consideration justifies the global result of a lower turbulence production for the sinusoidal riblets, as also evidenced in Cafiero et al. (2022).

3.5. Two-point correlations

The analysis of the effect of the surface manipulation on the wall-normal events is analysed by means of two-point correlations. Since the flow is not homogeneous in the wall normal direction, the two-point correlation coefficient between any two quantities R_{AB} was calculated as:

$$R_{AB} = \frac{\overline{A(x, y_{ref})B(x + \Delta x, y)}}{\sigma_A(y_{ref})\sigma_B(y)} \tag{3}$$

where y_{ref} is the reference wall-normal location at which the correlation is computed, Δx is the streamwise separation between A and B, σ_A is the standard deviation of A at y_{ref} and σ_B is the standard deviation of B at y. The value of $y_{ref}^+ = 50$ was selected for the present work since a change of y_{ref}^+ in the range between 25 and 80 wall units did not change significantly the shape of the correlation.

Figure 12 shows the R_{uu} and R_{uv} correlation coefficient calculated for the four investigated cases at $Re_\theta = 2900$ in the streamwise-wall normal plane. To improve the readability, one generic contour level is selected for all the cases: $R_{uu} = 0.6$ and $R_{uv} = -0.15$.

The effect of the riblet manipulation can be readily identified in both cases. In figure 12a the shape of the correlation coefficient R_{uu} already evidenced by Ganapathisubramani et al. (2005) for the smooth case suggests the presence of the hairpin structures that extend from the wall towards the log-layer. The surface manipulations cause a reduction of both the streamwise and the wall-normal extent of the correlation coefficient, thus suggesting a direct effect of the ribbed surface on the hairpin structures. In this sense, the most effective manipulation is the RS2 case, while RLONG and RS1 feature a very similar behaviour.

Similar conclusions can also be drawn from the R_{uv} correlation coefficient. The wall-normal extent of the correlation is indeed reduced for all the manipulated cases. The entity of the reduction is of about 8% for the RS2 case and 14% for the RLONG and RS1 cases, estimated as the maximum wall-normal extent of the correlation contour. Considering the negative value of the correlation coefficient R_{uv}, the low-speed streaks ($u' < 0$) are correlated with positive wall-normal events ($v' > 0$) (Ganapathisubramani et al., 2005). The attenuation of the wall-normal extent of the contours in the manipulated cases hence suggests that the riblet surface attenuates the exchange of momentum between the near wall region and the outer regions of the boundary layer.
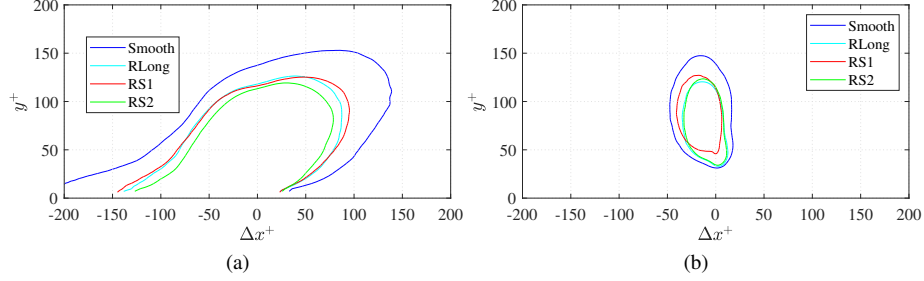
20

Figure 12: Contours of the two-point correlation coefficient R_{uu} (a) and R_{uv} (b) calculated for the four investigated cases in the Δx^+-y^+ plane at $y_{ref}^+ = 50$. To improve the plots' readability, one generic contour level is selected for all the cases: $R_{uu} = 0.6$ and $R_{uv} = -0.2$. In both figures, the flow is from left to right.

It is worth explicitly mentioning that the values of the correlation coefficients are quite similar between all the manipulated cases. This does not allow to draw conclusions on the differences introduced by the sinusoidal riblets with respect to the straight ones.

3.6. Detection of the near wall events

We performed conditional averages of the hot wire velocity signals to determine the effect of the geometry manipulation on the near wall events. We implemented the variable-interval temporal-averaging (VITA) technique (Blackwelder and Kaplan, 1976) to detect the occurrence of near wall events. The VITA average is defined for a generic quantity $Q(x, y, t)$ as

$$\hat{Q}(x, y, T) = \frac{1}{T} \int_{t-T/2}^{t+T/2} Q(x, y, s) ds \qquad (4)$$

where T indicates an averaging time. In the present case, the VITA technique is applied to determine a local variance, which is defined as

$$var_{loc}(x, y, t, T) = \hat{u'^2}(x, y, t, T) - (\hat{u'}(x, y, t, T))^2 \qquad (5)$$

where the $\hat{\ }$ indicates a local average, i.e. an average performed over the time interval T, which is typically set to $T^+ = 10$. The technique is readily applicable also to PIV data, provided that the time interval is replaced by a space interval, effectively obtaining the VISA (variable interval space averaging) technique.

The detection criterion dictates that an event is obtained when the value of the local variance $var_{loc}(x, y, t, T)$ exceeds by a factor k the value of the global variance ($\overline{u'^2} = \lim_{T \to \infty} var_{loc}$), that we set to $k = 1$. Among all those events that meet this criterion, we select those that are characterized by $du'/dt > 0$, that we can identify as acceleration events.
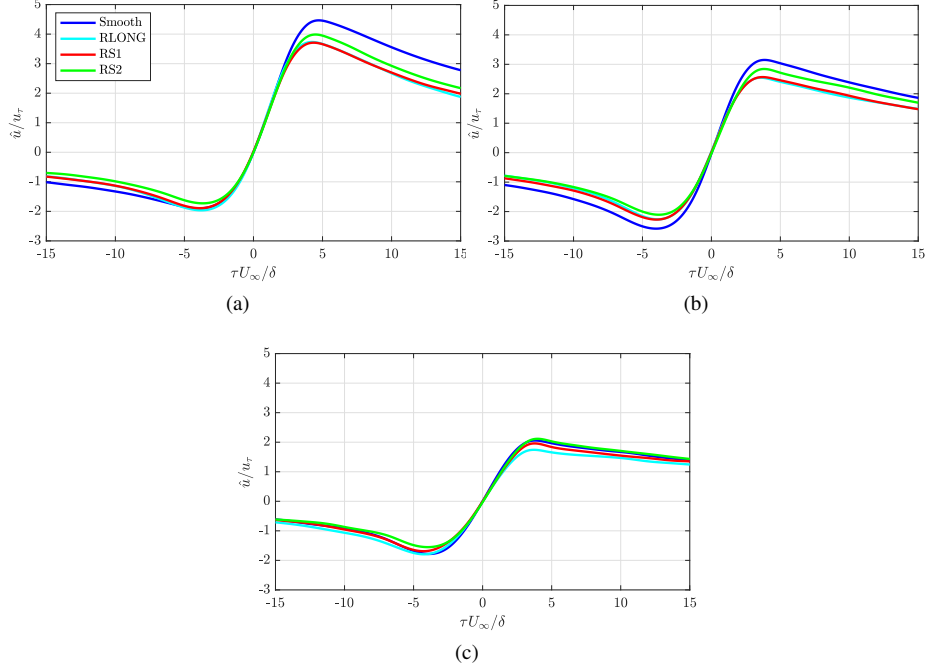
21

Figure 13: Conditionally averaged VITA event measured at a) $y^+ = 10$, b) $y^+ = 30$ and c) $y^+ = 100$ for the Smooth, RLONG, RS1 and RS2 cases. The data was collected at $Re_\theta = 3900$.

The time t_j where the previous conditions are met allows us to determine the conditionally averaged velocity signal as

$$\hat{u}(x, y, \tau) = \frac{1}{N} \sum_{j=1}^{N} u'(y, t_j + \tau) \tag{6}$$

where the time interval τ is conveniently defined to cover a range of realizations before and after the event. When events are detected at close temporal (or spatial, for the PIV case) distances, they are grouped and considered as one.

It is worth to explicitly mention that Blackwelder and Kaplan (1976) demonstrated that the conditionally averaged event is independent from the choice of the threshold k. For higher values of the threshold a longer time series is often needed to obtain a sufficiently converged conditional average. However, the statistical significance of the obtained result is demonstrated by the fact that the event scales with $k^{1/2}$.

Figure 13 shows the conditionally averaged VITA event expressed as $\hat{u}/u_\tau$, with u_τ being the friction velocity for the smooth plate. The data are plotted as a function of the non-dimensional time tU_∞/δ at a wall normal distance $y^+ = 10$ and for the representative case of $Re_\theta = 3900$.

The Smooth case exhibits the typical accelerating behaviour documented in the literature (Blackwelder and Kaplan, 1976). While the derivative near the origin of
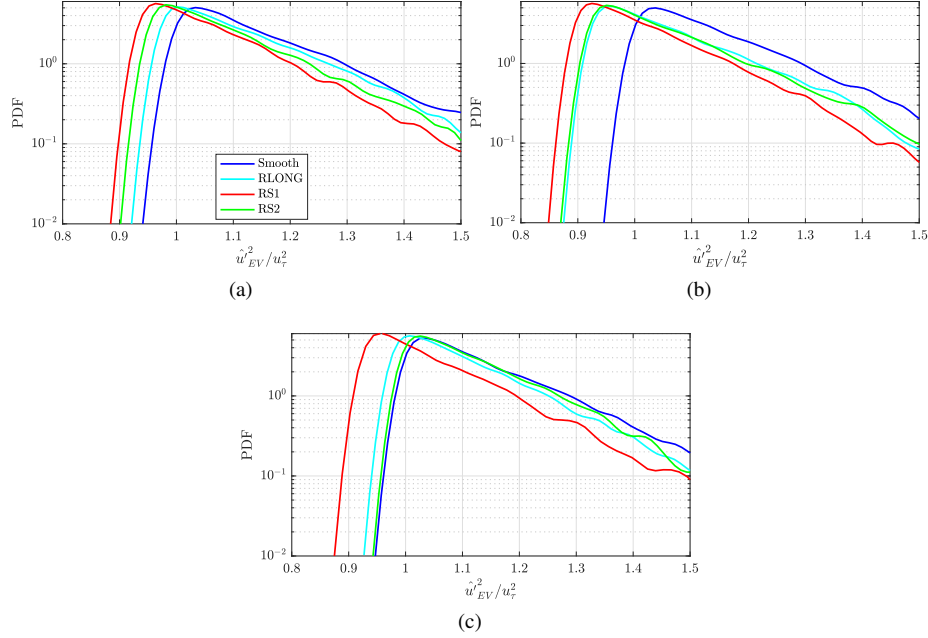
22

Figure 14: Conditional PDF of the streamwise velocity variance $\hat{u}^2_{EV}$ referred to the portions of the time history when a VITA event has been detected (a) $y^+ = 10$, b) $y^+ = 30$ and c) $y^+ = 100$). The data was collected at $Re_\theta = 3900$.

the conditional average is not significantly affected by the geometry manipulation, the peak to peak distance shows a consistently lower value for all the riblet cases. This is an indication that the geometry manipulation can lead to less intense events at small wall normal distances, in good agreement with the overall reduction of the turbulence intensity.

At larger values of the wall normal distance, $y^+ = 30$, the differences between the riblet geometries reduce, despite showing a smaller intensity with respect to the case at $y^+ = 10$ of the conditional event. As the wall normal distance increases, the differences fade out, with $y^+ = 100$ being the case where all the cases are practically overlapping, as also evidenced in Figure 6.

Figure 13 is instrumental in showing that the riblet geometry has indeed an effect on the near wall structure of the boundary layer. It is also important to stress that Iuso et al. (2002, 2003) using PIV measurements in the $x - z$ plane of a turbulent boundary layer showed that the VISA events associated with the wall normal vorticity are generally located at the edges of the high speed streaks. An attenuation in the intensity of these events is then associated with less intense coherent structures that populate the near wall region, thus tampering with the near wall turbulence production.

Besides providing a global description of the structure of the streamwise velocity variance, as reported in Figure 14, we focused on the share of the conditional variance associated with the events $\hat{u}^2_{EV}$ at three wall normal distances, $y^+ = 10, 30, 100$.

23

Starting from the identification criterion described above, we plotted the pdf of the streamwise velocity variance only conditioned on those portions of the time history that were identified as VITA events.

Independently from the wall normal location, the riblet surface guarantees a reduction of the velocity variance associated with the events. The results stemming from the analysis of Figure 14 suggest that independently from the distance from the wall the riblet geometry reduces the probability to find large values of the fluctuations, say $\hat{u}_{EV}^2/u_\tau^2 > 1$. This is particularly evident at $y^+ = 10$ and 30, where the most probable fluctuations are reduced by about 20% for the RS1 case. These results are also well aligned with the quadrant analysis shown in Figure 10.

Interestingly, while the intensity of the velocity fluctuations is roughly constant across the buffer layer for the Smooth plate, the manipulated surfaces evidence the highest reduction of the velocity variance close to the plate (Figure 14a,b). Similar conclusions were also drawn by Peet and Sagaut (2009) as it will be evidenced in the next section.

3.7. Manipulation mechanism

The presented data show an effect of the riblets on the near wall structure of the turbulent boundary layer. Nevertheless, a justification of the mechanism that drives the attenuation of the turbulence intensity associated with the sinusoidal riblets is not completely clear yet. We try and explain this aspect linking the wavy geometry of the wall to the active control technique presented in the introduction, namely the spanwise wall oscillation, in a similar fashion to Peet and Sagaut (2009). In fact, the authors suggested that the additional turbulence suppression catered by the sinusoidal riblets is due to tilting of the streawise vortices that loose their spatial coherence. This active technique yields significant attenuation of the turbulence intensity and related drag reduction, and the leading mechanism is related to the effect that the spanwise motion has on the stability of the streaks.

Choi (2002), along with others, attributed the beneficial effect of the spanwise oscillations to the tilting of the vortex sheet in the Stokes layer in the spanwise direction that originate negative spanwise vorticity; this effect reduces the streamwise velocity in the near wall region, thus reducing the wall normal velocity gradients. More recently, Leschziner (2020) and Agostini et al. (2021) investigating the channel flow subject to spanwise oscillations linked the drag-reduction effectiveness of oscillatory spanwise wall motion to the strongly asymmetric response of the production rate and the turbulence level in the buffer layer to positive against negative footprints, the former strongly enhancing small-scale turbulence.

To determine if the signature of the wavy wall is felt across the near wall region, we focus on the conditionally averaged spanwise velocity measured with the Stereo-PIV data.

A similar detection criterion to the one described above (eq.5-6) is applied to the Stereo-PIV data, but in this case when detecting a VISA event, we look at the conditional average of the spanwise velocity component, $\hat{w}$, as a function of the streamwise distance.

The conditionally averaged spanwise velocity, $\hat{w}$, reported in Figure 15 shows larger intensity for the sinusoidal riblets at both $y^+ = 20$ (a) and $y^+ = 30$ (b). It is
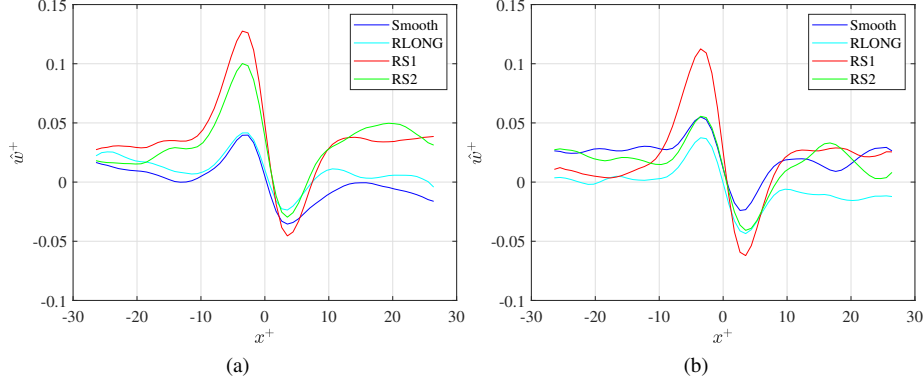
Figure 15: Conditionally averaged $\hat{w}$ determined using the VISA technique for the Smooth, RLONG, RS1 and RS2 cases. The data was collected at a) $y^+ = 20$ and b) $y^+ = 30$ at a value of the Reynolds number $Re_\theta = 3900$.

worth to explicitly mention that the value $\hat{w}$ is expected to be non-zero also for the flat plate and the longitudinal riblets since the near wall structures are inherently three dimensional. The sinusoidal riblets induce a further share of spanwise oscillation very close to the wall, that is expected to be amplified when a VISA event takes place.

At $y^+ = 20$, a clear difference between the sinusoidal and non-sinusoidal cases can be detected, with the values of $\hat{w}$ being quite similar between the Smooth and the RLONG cases. Conversely, the sinusoidal pattern of the grooves shows a clear signature in the values of $\hat{w}$. It is interesting to see that the RS1 case, despite being characterized by a smaller amplitude a, features larger values of the spanwise oscillation. This can be attributed to the interplay between the spanwise induced motion and the local blockage imposed on the flow by the groove (being the sinusoidal riblet at an angle with respect to the freestream), which would in turn justify the non monotonic behaviour of the spanwise motion with the amplitude. Nevertheless, a broader parametric space is needed to confirm this consideration.

A closer inspection of Figure 15 also suggests that at $y^+ = 20$, where both the sinusoidal riblet cases cater for a larger peak to peak value of $\hat{w}$, the slope of the conditional event is much steeper than the RLONG and Smooth cases. At larger distances from the wall, $y^+ = 30$, the RS1 keeps the same slope of conditioned spanwise velocity $\hat{w}$ evidenced at $y^+ = 20$. On the other hand, the RS2 features a reduction of the slope of the conditioned event, attaining the same values of the RLONG and the Smooth cases.

Estimating the peak to peak distance in the four investigated cases, at $y^+ = 30$ it is possible to see that the RLONG provides values to within 6% of the Smooth case, while the sinusoidal riblets are responsible for a significantly larger $\hat{w}$, respectively 23% and 132% for the RS2 and RS1 cases at $y^+ = 30$. This result seems to be aligned with the picture of spanwise induced motion that reflects the signature of the wall roughness across the boundary layer.

The previous observations find also some similarities with the behaviour that characterizes the meandering in rivers, despite the significant difference in the friction
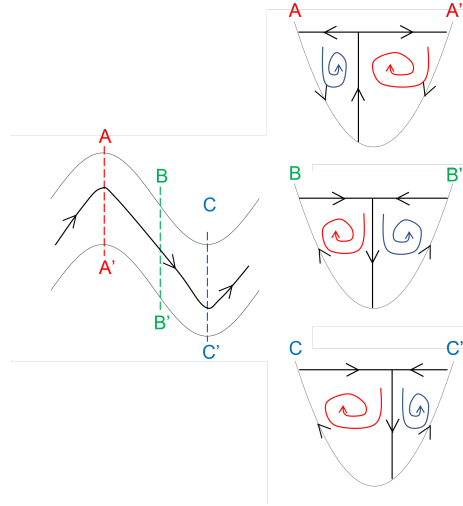
25

Figure 16: Schematic representation of the secondary flows due to the sinuous riblet. Figure re-adapted from Hey and Thorne (1975). Red and blue spirals are representative of positive and negative vorticity, respectively.

Reynolds number. In particular, Hey and Thorne (1975) reported a qualitative model of the secondary flow behaviour in sinuous rivers in terms of spiral cells.

In the present case, within the grooves the flow evolves in the viscous regime following the path of the riblets channel. The sinuous geometry could originate secondary flows due to the alternate bending of the groove in a similar fashion to sinuous rivers, as schematically represented in Figure 16. These secondary flows are characterized by counter rotating sinuous vortices that vary their size and vorticity magnitude along the grooves (Hey and Thorne, 1975). More importantly, the inversion of the vorticity sign at each bend gives rise to a spatially inhomogeneous spanwise sheet of vorticity.

It can then be argued that the flow in the very proximity of the grooves is manipulated by the underlying *sinuous river riblets flows*. This inhomogeneous vorticity layer tends to modify the streaky structures very close to the wall weakening and/or disrupting them, thus tampering with the wall turbulence regeneration mechanism.

In conclusion, the mean transverse velocity $\hat{w}$ generated by the sinuous riblets could behave similarly to the active forcing case, thus following the spanwise wall oscillation, with the additional effect of the small scale varying sinuous vorticity.

It is important to point out that the model described here will need further investigation, via both numerical and experimental analysis, in order to reveal the interplay between the sinusoidal groove and the buffer layer, leading to the drag reduction evidenced in Figure 4.

4. Conclusions

In this manuscript we have provided statistical evidence of the effect of sinusoidal riblets to tamper with the near wall structures in a turbulent boundary layer using ma-

nipulated surfaces with a number of wavelengths of the grooves up to 13, corresponding to a number of boundary layer thickness (δ) ranging from 6 to 10.

The load cell measurements have provided evidence of drag reduction. This is confirmed both against the smooth case and, more importantly, against the straight micro-grooves. It is evidenced how the sinusoidal geometry retains the main features of the longitudinal ones, with a peak in the drag reduction that is a function of the grooves' spacing normalised in inner units.

The mean and the variance of the streamwise velocity evidence an upward shift in the logarithmic region and an attenuation of the turbulence intensity peak, respectively. A consistent behaviour is also confirmed by the Reynolds shear stresses.

The comparison of the velocity spectra shows an attenuation of the near-wall energy in the range of $y^+ < 100$ and for a wide range of wavelengths, λ_x^+. This suggested that the energy distribution across the different scales is influenced by the surface conditions, and that this effect is most significant in the near-wall region.

The investigation also highlighted a possible mechanism, that is related to the signature of the sinusoidal pattern on the flow field near the wall. From the analysis of the VITA and VISA events, it is indeed shown that the riblet geometry enhances the spanwise meandering of the near wall structures, yielding a weakening of the turbulence production cycle. Conversely, the streamwise events are attenuated, at least at wall normal distances of interest for the turbulence production. The differences with the Smooth boundary layer and the RLONG case fade out as the wall normal distance increases.

The study of the two-point correlation coefficient shows that the sinsuoidal riblets have an effect on both the streamwise extent and the wall-normal penetration of the R_{uu} correlation, thus suggesting an effect on the near-wall streaky structures. Furthermore, the correlation coefficient R_{uv} evidences a decorrelation introduced by the ribbed surfaces on the wall normal velocity fluctuations related to the low-speed streaks.

The quadrant analysis also confirms these observations, with the sinusoidal geometries being characterized by a lower correlation between the streamwise and wall normal velocity fluctuations; furthermore, the pre-multiplied jPDF ($-u'v'P(u'v')$) also suggest that the velocity fluctuations that contribute the most to the turbulence production for the sinusoidal cases are generally lower than the Smooth and RLONG cases. This is in good agreement with the overall picture of a near wall cycle with less turbulence production.

The enhancement in performance of the sinusoidal riblets with respect to the straight ones might find a possible explanation to the existence of secondary flows that develop inside the sinusoidal grooves, with the production of secondary near wall structures with alternating vorticity sign. These secondary flows could be responsible for the weakening and fragmentation of the typical flow structures developing in the near wall region just above the grooves and that are responsible for the turbulence regeneration mechanism. It must be noted that further investigations are needed to support this proposed possible mechanism.

Moreover, it is not immediately possible to draw conclusions on the effect of the amplitude a of the sinusoidal pattern from the current investigation. A broader parametric space would be needed to confirm that there is indeed an effect and how this participates into the drag reduction mechanism.

Acknowledgement

References

Agostini, L., Leschziner, M., Agostini, L., Leschziner, M.A., 2021. Statistical analysis of outer large-scale/inner-layer interactions in channel flow subjected to oscillatory drag-reducing wall motion using a multiple-variable joint-probability-density function methodology. Journal of Fluid Mechanics 923, 25. doi:10.1017/JFM.2021.585.

Airbus, 2019. Famos project at the zal. URL: https://old.future.hamburg/en/project/famos-project-at-the-zal/.

Astarita, T., 2006. Analysis of interpolation schemes for image deformation methods in PIV: Effect of noise on the accuracy and spatial resolution. Experiments in Fluids 40, 977–987. doi:10.1007/s00348-006-0139-4.

Astarita, T., 2007. Analysis of weighting windows for image deformation methods in PIV. Experiments in Fluids 43, 859–872. doi:10.1007/s00348-007-0314-2.

Astarita, T., 2008. Analysis of velocity interpolation schemes for image deformation methods in PIV. Experiments in Fluids 45, 257–266. doi:10.1007/s00348-008-0475-7.

Baron, A., Quadrio, M., Vigevano, L., 1993. On the boundary layer/riblets interaction mechanisms and the prediction of turbulent drag reduction. International Journal of Heat and Fluid Flow 14, 324–332. doi:10.1016/0142-727X(93)90005-8.

Bechert, D.W., Bartenwerfer, M., 1989. The viscous flow on surfaces with longitudinal ribs. Journal of Fluid Mechanics 206, 105–129. doi:10.1017/S0022112089002247.

Bechert, D.W., Bruse, M., Hage, W., 2000. Experiments with three-dimensional riblets as an idealized model of shark skin. Experiments in Fluids 28, 403–412. doi:10.1007/s003480050400.

Bechert, D.W., Bruse, M., Hage, W., Van Der Hoeven, J.G., Hoppe, G., 1997. Experiments on drag-reducing surfaces and their optimization with an adjustable geometry. Journal of Fluid Mechanics 338, 59–87. doi:10.1017/S0022112096004673.

Bechert, D.W., Hoppe, G., Reif, W.E., 1985. On the drag reduction of the shark skin, in: AlAA 23rd Aerospace Sciences Meeting, 1985. doi:10.2514/6.1985-546.

Blackwelder, R.F., Kaplan, R.E., 1976. On the wall structure of the turbulent boundary layer. Journal of Fluid Mechanics 76, 89–112. doi:10.1017/S0022112076003145.

Cafiero, G., Amico, E., Iuso, G., 2022. Wall bounded flows manipulation using sinusoidal riblets. AIAA Science and Technology Forum and Exposition, AIAA SciTech Forum 2022 doi:10.2514/6.2022-0709.

Cannata, M., Cafiero, G., Iuso, G., 2020. Large-scale forcing of a turbulent channel flow through Spanwise synthetic jets. AIAA Journal 58, 2042–2052. doi:10.2514/1.J059047.

Cerutti, J.J., Sardu, C., Cafiero, G., Iuso, G., 2020. Active flow control on a square-back road vehicle. Fluids 5. doi:10.3390/fluids5020055.

Choi, H., Moin, P., Kim, J., 1993. Direct numerical simulation of turbulent flow over riblets. Journal of Fluid Mechanics 255, 503–539. doi:10.1017/S0022112093002575.

Choi, K.S., 1989. Near-wall structure of a turbulent boundary layer with riblets. Journal of Fluid Mechanics 208, 417–458. doi:10.1017/S0022112089002892.

Choi, K.S., 2002. Near-wall structure of turbulent boundary layer with spanwise-wall oscillation. Physics of Fluids 14, 2530–2542. doi:10.1063/1.1477922.

De Graaff, D.B., Eaton, J.K., 2000. Reynolds-number scaling of the flat-plate turbulent boundary layer. Journal of Fluid Mechanics 422, 319–346. doi:10.1017/S0022112000001713.

Di Cicca, G.M., Iuso, G., Spazzini, P.G., Onorato, M., 2002a. Particle image velocimetry investigation of a turbulent boundary layer manipulated by spanwise wall oscillations. Journal of Fluid Mechanics 467, 41–56. doi:10.1017/S002211200200157X.

Di Cicca, G.M., Iuso, G., Spazzini, P.G., Onorato, M., 2002b. PIV study of the influence of large-scale streamwise vortices on a turbulent boundary layer. Experiments in Fluids 33, 663–669. doi:10.1007/s00348-002-0510-z.

FreightWaves, 2021. Lufthansa replicates sharkskin to boost fuel efficiency of cargo jets.

Ganapathisubramani, B., Hutchins, N., Hambleton, W.T., Longmire, E.K., Marusic, I., 2005. Investigation of large-scale coherence in a turbulent boundary layer using two-point correlations. Journal of Fluid Mechanics 524, 57–80. doi:10.1017/S0022112004002277.

García-Mayoral, R., Jiménez, J., 2011. Drag reduction by riblets. Philosophical Transactions of the Royal Society A: Mathematical, Physical and Engineering Sciences 369, 1412–1427. doi:10.1098/rsta.2010.0359.

Gehlert, P., Cherfane, Z., Cafiero, G., Vassilicos, J.C., 2021. Effect of multiscale endplates on wing-tip vortex. AIAA Journal 59. doi:10.2514/1.J059878.

Giordano, R., Astarita, T., 2009. Spatial resolution of the Stereo PIV technique. Experiments in Fluids 46, 643–658. doi:10.1007/s00348-008-0589-y.

Hambleton, W.T., Hutchins, N., Marusic, I., 2006. Simultaneous orthogonal-plane particle image velocimetry measurements in a turbulent boundary layer. Journal of Fluid Mechanics 560, 53–64. doi:10.1017/S0022112006000292.

Herpin, S., Stanislas, M., Foucaut, J.M., Coudert, S., 2013. Influence of the reynolds number on the vortical structures in the logarithmic region of turbulent boundary layers. Journal of Fluid Mechanics 716, 5–50. doi:10.1017/JFM.2012.491.

Hey, R.D., Thorne, C.R., 1975. Secondary flows in river channels. Area 7, 191–195.

Hutchins, N., Nickels, T.B., Marusic, I., Chong, M.S., 2009. Hot-wire spatial resolution issues in wall-bounded turbulence. Journal of Fluid Mechanics 635, 103–136. doi:10.1017/S0022112009007721.

Ibrahim, J.I., Gómez-De-Segura, G., Chung, D., García-Mayoral, R., 2021. The smooth-wall-like behaviour of turbulence over drag-altering surfaces: A unifying virtual-origin framework. Journal of Fluid Mechanics 915, 1–39. doi:10.1017/jfm.2021.13, arXiv:2006.16118.

Iuso, G., Di Cicca, G.M., 2007. Interaction of synthetic jets with a fully developed turbulent channel flow. Journal of Turbulence 8, 1–33. doi:10.1080/14685240601110088.

Iuso, G., Di Cicca, G.M., Onorato, M., Spazzini, P.G., Malvano, R., 2003. Velocity streak structure modifications induced by flow manipulation. Physics of Fluids 15, 2602–2612. doi:10.1063/1.1597680.

Iuso, G., Onorato, M., 1995. Turbulent boundary layer manipulation by outer-layer devices. Meccanica 30, 359–376. doi:10.1007/BF00993419.

Iuso, G., Onorato, M., Spazzini, P.G., Di Cicca, G.M., 2002. Wall turbulence manipulation by large-scale streamwise vortices. Journal of Fluid Mechanics , 23–58doi:10.1017/S0022112002002574.

Ji, Y., Yao, J., Hussain, F., Chen, X., 2021. Vorticity transports in turbulent channels under large-scale control via spanwise wall jet forcing. Physics of Fluids 33, 095112. doi:10.1063/5.0062937.

Jimenez, J., 2004. Turbulent Flows Over Rough Walls. Annual Review of Fluid Mechanics 36, 173–196. doi:10.1146/annurev.fluid.36.050802.122103.

Kramer, F., Gruneberger, R., Thiele, F., E., W., Hage, W., Meyer, R., 2010. Wavy riblets for turbulent drag reduction, in: 5th AIAA Flow Control Conference. doi:10.2514/6.2010-4583.

Lee, S., Ayton, L., Bertagnolio, F., Moreau, S., Chong, T.P., Joseph, P., 2021. Turbulent boundary layer trailing-edge noise: Theory, computation, experiment, and application. Progress in Aerospace Sciences 126, 100737. doi:10.1016/J.PAEROSCI.2021.100737.

Leschziner, M.A., 2020. Friction-drag reduction by transverse wall motion – a review. Journal of Mechanics 36, 649–663. doi:10.1017/JMECH.2020.31.

Luchini, P., 1993. Viscous sublayer analysis of riblets and wire arrays. Applied Scientific Research 50, 255–266. doi:10.1007/BF00850560.

Luchini, P., Manzo, F., Pozzi, A., 1991. Resistance of a grooved surface to parallel flow and cross-flow. Journal of Fluid Mechanics 228, 87–109. doi:10.1017/S0022112091002641.

Luchini, P., Manzo, F., Pozzi, A., 1992. Viscous eddies over a grooved surface computed by a Gaussian-integration Galerkin boundary-element method. AIAA Journal 30, 2168–2170. doi:10.2514/3.11200.

Luchini, P., Trombetta, G., 1995a. Effects of riblets upon flow stability. Applied Scientific Research 54, 313–321. doi:10.1007/BF00863516.

Luchini, P., Trombetta, G., 1995b. Effects of riblets upon flow stability. Applied Scientific Research 54, 313–321. doi:10.1007/BF00863516.

Mamori, H., Yamaguchi, K., Sasamori, M., Iwamoto, K., Murata, A., 2019. Dual-plane stereoscopic PIV measurement of vortical structure in turbulent channel flow on sinusoidal riblet surface. European Journal of Mechanics, B/Fluids 74, 99–110. doi:10.1016/j.euromechflu.2018.11.006.

Marusic, I., Chandran, D., Rouhi, A., Fu, M.K., Wine, D., Holloway, B., Chung, D., Smits, A.J., 2021. An energy-efficient pathway to turbulent drag reduction. Nature Communications 2021 12:1 12, 1–8. doi:10.1038/s41467-021-26128-8.

Mele, B., Russo, L., Tognaccini, R., 2020a. Drag bookkeeping on an aircraft with riblets and nlf control. Aerospace Science and Technology 98, 105714. doi:10.1016/J.AST.2020.105714.

Mele, B., Tognaccini, R., Catalano, P., Rosa, D.D., 2020b. Effect of body shape on riblets performance. Physical Review Fluids 5, 124609. doi:10.1103/PHYSREVFLUIDS.5.124609/FIGURES/9/MEDIUM.

Mendez, M.A., Raiola, M., Masullo, A., Discetti, S., Ianiro, A., Theunissen, R., Buchlin, J.M., 2017. POD-based background removal for particle image velocimetry. Experimental Thermal and Fluid Science 80, 181–192. doi:10.1016/j.expthermflusci.2016.08.021.

Modesti, D., Endrikat, S., Hutchins, N., Chung, D., 2021. Dispersive stresses in turbulent flow over riblets. Journal of Fluid Mechanics 917, A55. doi:10.1017/jfm.2021.310.

NASA, 1993. Nasa riblets for stars & stripes. URL: https://www.nasa.gov/centers/langley/news/factsheets/Riblets.html.

Peet, Y., Sagaut, P., 2009. Theoretical prediction of turbulent skin friction on geometrically complex surfaces. Physics of Fluids 21. doi:10.1063/1.3241993.

Peet, Y., Sagaut, P., Charron, Y., 2008. Turbulent drag reduction using sinusoidal riblets with triangular cross-section, in: 38th AIAA Fluid Dynamics Conference and Exhibit. doi:10.2514/6.2008-3745.

Quadrio, M., 2011. Drag reduction in turbulent boundary layers by in-plane wall motion. Philosophical Transactions of the Royal Society A: Mathematical, Physical and Engineering Sciences 369, 1428–1442. doi:10.1098/rsta.2010.0366.

Quadrio, M., Ricco, P., 2004. Critical assessment of turbulent drag reduction through spanwise wall oscillations. Journal of Fluid Mechanics 521, 251–271. doi:10.1017/S0022112004001855.

Sasamori, M., Iihama, O., Mamori, H., Iwamoto, K., Murata, A., 2017. Parametric Study on a Sinusoidal Riblet for Drag Reduction by Direct Numerical Simulation. Flow, Turbulence and Combustion 99, 47–69. doi:10.1007/s10494-017-9805-2.

Sasamori, M., Mamori, H., Iwamoto, K., Murata, A., 2014. Experimental study on drag-reduction effect due to sinusoidal riblets in turbulent channel flow. Experiments in Fluids 55. doi:10.1007/s00348-014-1828-z.

Schoppa, W., Hussain, F., 1998a. A large-scale control strategy for drag reduction in turbulent boundary layers. Physics of Fluids 10, 1049–1051. doi:10.1063/1.869789.

Schoppa, W., Hussain, F., 1998b. Genesis of longitudinal vortices in near-wall turbulence. Meccanica 33, 489–501. doi:10.1023/A:1004320610285.

Sha, T., Itoh, M., Tamano, S., Yokota, K., Akio, N., 2005. 207 Experimental Study on Drag Recduction in Turbulent Flow on Zigzag Riblet Surface. The Proceedings of the Fluids engineering conference 2005, 21. doi:10.1299/jsmefed.2005.21.

Spalart, P.R., Mclean, J.D., 2011. Drag reduction: Enticing turbulence, and then an industry. Philosophical Transactions of the Royal Society A: Mathematical, Physical and Engineering Sciences 369, 1556–1569. doi:10.1098/rsta.2010.0369.

Tsai, R.Y., 1987. A Versatile Camera Calibration Technique for High-Accuracy 3D Machine Vision Metrology Using Off-the-Shelf TV Cameras and Lenses. IEEE Journal on Robotics and Automation 3, 323–344. doi:10.1109/JRA.1987.1087109.

Wallace, J.M., 2016. Quadrant Analysis in Turbulence Research: History and Evolution. Annual Review of Fluid Mechanics 48, 131–158. doi:10.1146/annurev-fluid-122414-034550.

Walsh, M., 1980. Drag Characteristics of V-Groove and Transverse Curvature Riblets, in: Viscous Flow Drag Reduction, pp. 168–184. doi:10.2514/5.9781600865466.0168.0184.

Walsh, M., 1982. Turbulent boundary layer drag reduction using riblets. AIAA Journal 82, 0169. doi:10.2514/6.1982-169.

Walsh, M.J., 1983. Riblets as a viscous drag reduction technique. AIAA Journal 21, 485–486. doi:10.2514/3.60126.

Walsh, M.J., Anders, J.B., 1989. Riblet/lebu research at nasa langley. Applied Scientific Research 1989 46:3 46, 255–262. doi:10.1007/BF00404822.

Wieneke, B., 2005. Stereo-PIV using self-calibration on particle images. Experiments in Fluids 39, 267–280. doi:10.1007/s00348-005-0962-z.

Wieneke, B., 2018. Improvements for volume self-calibration. Measurement Science and Technology 29. doi:10.1088/1361-6501/aacd45.

Willert, C., 1997. Stereoscopic digital particle image velocimetry for application in wind tunnel flows. Measurement Science and Technology 8, 1465–1479. doi:10.1088/0957-0233/8/12/010.

Yao, J., Chen, X., Hussain, F., 2018. Drag control in wall-bounded turbulent flows via spanwise opposed wall-jet forcing. Journal of Fluid Mechanics 852, 678–709. doi:10.1017/jfm.2018.553.

Yao, J., Chen, X., Hussain, F., 2021. Composite active drag control in turbulent channel flows. Physical Review Fluids 6, 054605. doi:10.1103/PHYSREVFLUIDS.6.054605/FIGURES/10/MEDIUM.